Nanoscale

Accepted Manuscript

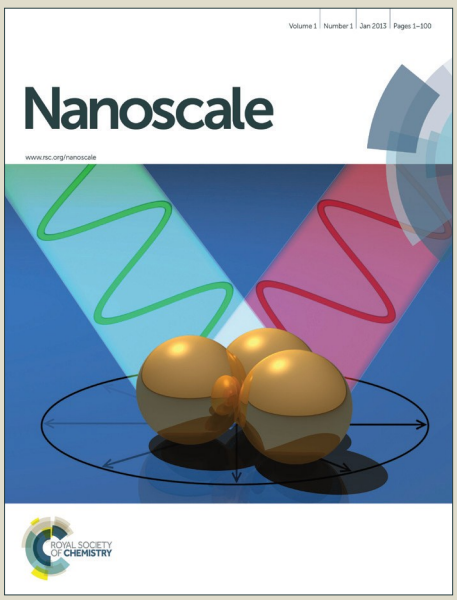

ROYAL SOCIETY OF CHEMISTRY

www.rsc.org/nanoscale

Journal Name

RSCPublishing

ARTICLE

Conducting additive-free amorphous GeO_2/C composite as a high capacity and long-term stability anode for lithium ion batteries

Cite this: DOI: 10.1039/x0xx00000x

Received 00th January 2012,
Accepted 00th January 2012

DOI: 10.1039/x0xx00000x

www.rsc.org/

Duc Tung Ngo, Ramchandra S. Kalubarme, Hang T.T. Le, Choong-Nyeon Park and Chan-Jin Park*

In the present study, a novel method has been proposed to synthesize amorphous GeO_2/C composite. The amorphous GeO_2/C composite, without carbon black as the electrode for the Li-ion battery, exhibited a high specific capacity of 914 mA h g^{-1} under the C/2 rate and an enhanced rate capability. The amorphous GeO_2/C electrode presented excellent electrochemical stability with a 95.3% charge capacity retention after 400 charge-discharge cycles, even under a high current charge-discharge of C/2. Furthermore, the full cell employing the GeO_2/C anode and the $LiCoO_2$ cathode displayed outstanding cycling performance. The superior performance of the GeO_2/C electrode enables the amorphous GeO_2/C to be a promising anode material for Li-ion secondary batteries.

Introduction

Nowadays, fully charged electric vehicles employing lithium ion batteries (LIBs) can only run up to 150 km, which does not satisfy the customer's requirement for longer driving distances. Increasing the specific capacity of the anode in LIB is one of the attractive routes to improve the energy density of LIB. Many attempts have been made to develop alternative anode materials such as metal or metal-based oxides to make lithium alloys,[1-14] conversion oxides,[15-18] and intercalation compounds[19, 20] to conventional graphite. Among these attempts, metal-based oxides used to make nano-sized lithium alloys have attracted much attention. In particular, germanium dioxide (GeO_2), which possesses a high theoretical capacity of 1100 mA h g^{-1}, is approximately three times higher than the specific capacity of commercial graphite (372 mA h g^{-1}).[7, 21, 22] In addition, it can exhibit a low potential plateau and high Li diffusivity.[23, 24] However, the GeO_2 anode undergo considerably large volume change during the lithiation and de-lithiation processes.[25, 26] This significant volume change can result in pulverization of the active materials, leading to electronic isolation. Further, the fragmentation of active materials can finally induce the capacity fading of the electrode. The structural change of GeO_2 almost occurs at the first cycle when GeO_2 reacts with lithium to form an amorphous structure of Ge and Li_2O.[26] This change in structure of GeO_2 from crystalline to amorphous as well as the volume expansion during the alloying step is the main cause of the capacity fading of the GeO_2 electrode.

Many researchers have focused on solving the volume expansion problem to mitigate the capacity fading of the GeO_2 electrode. The most popular solutions for this problem are the use of carbon as a buffer layer to mitigate the considerably large volume expansion [6, 27-30] and the use of an amorphous material [31] to prevent the change in structure during the charge-discharge process. The use of an amorphous material can prevent the structure failure, caused by anisotropic expansion.[32] However, the use of carbon as a buffer layer slightly reduces the capacity of the total material due to the reduced weight content of the active material in the electrode. Carbon black has been well established as a conductive additive for electrode materials in order to improve the conductivity of the electrode.[33, 34] Normally, the electrodes are fabricated by mixing an active material, carbon black, and a binder at a weight ratio of 8:1:1, respectively. Therefore, the capacity calculated based on the total weight of the electrode decreases significantly due to the reduction in the actual weight of the active material on the electrode.[35-37] A new strategy is introduced in this study, in which the carbon component plays two roles, as a buffer layer and a conductive additive. The used carbon acts not only as a buffer layer to improve the cyclability, but also as a conductive additive. This will reduce the additional usage of carbon as a conductive additive and hence increase the total weight of active materials on the electrode. The carbon buffer layer together with amorphous GeO_2 will accommodate the volume expansion. Therefore, the capacity and cyclability of the electrode will be increased. Particularly, in this paper, we reported the one-pot synthesis of amorphous GeO_2/C material using the citric-gel method. The distribution of amorphous GeO_2 in the carbon buffer layer has shown excellent cyclability when electrodes are fabricated without carbon black.

Experimental

Synthesis of GeO_2/C composite

Amorphous GeO_2 nano particles embedded in a carbon buffer matrix were synthesized using the citric method. The complex of germanium and citrate was prepared using GeO_2, citric acid and NH_4OH as the main starting chemicals. All chemicals were supplied by Sigma-Aldrich and used without further purification. Firstly, 0.5M germanate $Ge(OH)_4$ solution was prepared by dissolved GeO_2 in deionized (DI) water with the drop-wise addition of NH_4OH until a transparent solution was obtained. This solution was then added gradually to a 1M citric acid solution. In the resultant mixture, the molar ratio of citric acid:GeO_2 = 2:1. Further, the pH of the mixture solution was adjusted to 3.6 by adding NH_4OH to yield a germanium complex. The germanium complex was decomposed at 400 °C for 3 h in air to control the carbon content and then annealed at 700 °C in an argon atmosphere for 30 min to increase the graphitization of carbon. The enhanced degree of graphitization can improve the electronic conductivity of carbon and hence the performance of the electrode. Hereafter, the obtained product before and after graphitization are denoted as "as-prepared GeO_2/C" and "GeO_2/C", respectively. The pyrolytic carbon was prepared by carbonized the citric acid at 700 °C in an argon atmosphere for 30 min.

Structural characterization

An X-ray diffractometer (XRD; D/MAX Ultima III, Rigaku, Japan) with Cu Kα radiation was used to analyse the crystal structure of the synthesized materials. X-ray photoelectron spectroscopy (XPS; MultiLab2000, VG) and Raman spectroscopy (Horiba Jobin-Yvon, France) with an excitation light source of a 514 nm diode laser were used to investigate the chemical state of the materials. Fourier transform infrared spectroscopy (FTIR, IR Prestige-21, Shimadzu, Japan) is also used to examine the chemical state of the materials. Thermo-gravimetric analysis (TGA; TGA-50 Shimadzu instrument) of the materials was carried out from room temperature to 1000 °C with a ramp of 10 °C min^{-1}. Nitrogen adsorption and desorption isotherms (ASPA 2020, Micromeritics USA) for the materials were measured at -196 °C to estimate the specific area of the materials. The specific surface area of the samples was calculated using the Brunauer-Emmett-Teller (BET) method. The microstructure of the samples was observed using scanning electron microscopy (SEM, S-4700/EX-200, Hitachi) and transmission electron microscopy-Energy dispersive X-ray spectroscopy (TEM-EDS, Tecnai G_2, Philips).

Electrochemical characterization

To investigate the electrochemical characteristics of amorphous GeO_2/C composite, the electrodes were fabricated using a slurry casting process with and without carbon black as a conductive additive for comparison. Slurry casting with carbon black was prepared by mixing GeO_2/C : carbon black : binder with the weight ratio of 8:1:1, and that without carbon black was prepared by blending GeO_2/C : binder with the weight ratio of 9:1. A solution of 1 M $LiPF_6$ dissolved in ethylene carbonate (EC) and dimethyl carbonate (DMC) at a volume ratio of 1:1, with a small amount (3 wt%) of fluoroethylene carbonate (FEC), was used as the electrolyte. In order to distinguish from the electrode prepared with GeO_2/C, the electrode fabricated with the mixture of "GeO_2/C" and carbon black was denoted as "CB-GeO_2/C". The electrochemical properties of the obtained electrodes were investigated using cyclic voltammetry (CV) in the potential range of 0.0 to 3.0 V vs. Li/Li^+ at a scan rate of 0.05 mV s^{-1} with a Potentiostat (Gamry - PC750). In addition, the cells were galvanostatic charged and discharged from 0.01 to 1.50 V vs. Li/Li^+ using an automatic battery cycler (WonATech-WBCS 3000). All experiments and tests were conducted at 25 °C.

Results and Discussion

Fig. 1a presents the X-ray diffraction pattern of the GeO_2/C and pyrolytic carbon. The XRD pattern of GeO_2/C showed a broad peak with low intensity at $2\theta \approx 23.8°$ is attributed to the presence of pyrolytic carbon. Any additional peak corresponding to crystalline GeO_2 was not seen in the XRD pattern suggesting the amorphous state. Furthermore, the XPS spectrum of the sample shown in Fig. 1b indicated that Ge in the material had an oxidation state of +4, corresponding to a binding energy of 32.4 eV. From the XRD and XPS results, it can be concluded that the obtained product contained amorphous germanium dioxide (GeO_2). In addition, the Fourier transform infrared spectroscopy (FTIR) of GeO_2/C in Fig. S1†, yet again established the presence of GeO_2. The FTIR spectrum of GeO_2/C shows a band at 876 cm^{-1} corresponding to the vibration mode of GeO_4 tetrahedra.[38] To further establish the presence and graphitization of carbon in the synthesized product, the as-prepared GeO_2/C and GeO_2/C samples were analysed using Raman spectroscopy. As can be clearly seen in Fig. S2† & Fig. 1c, the Raman spectra consisted of two peaks at ~ 1350 and ~ 1560 cm^{-1}, corresponding to the disorder-induced D band and graphitic G band of carbon, respectively.[39] The intensity ratio of G band to D band (I_D/I_G) of GeO_2/C sample before and after graphitization was about 1.08 (Fig. S2†) and 0.96 (Fig. 1c), respectively. Therefore, obtained Raman spectroscopy results showed that after annealing at 700 °C the graphitization degree of carbon in GeO_2/C increased significantly. The carbon content in the GeO_2/C was determined using thermo-gravimetric analysis (TGA). As shown in Fig. 1d, the weight loss that was induced by the loss of carbon content was estimated to be 13.5 wt%.

Fig. 1 (a) X-ray diffraction pattern of GeO_2/C and pyrolytic carbon, respectively ; (b) Ge 3d XP spectra; (c) Raman spectra; (d) thermo-gravimetric analysis of GeO_2/C.

To determine the specific surface area of the obtained GeO_2/C, N_2 adsorption/desorption isotherms of the samples were

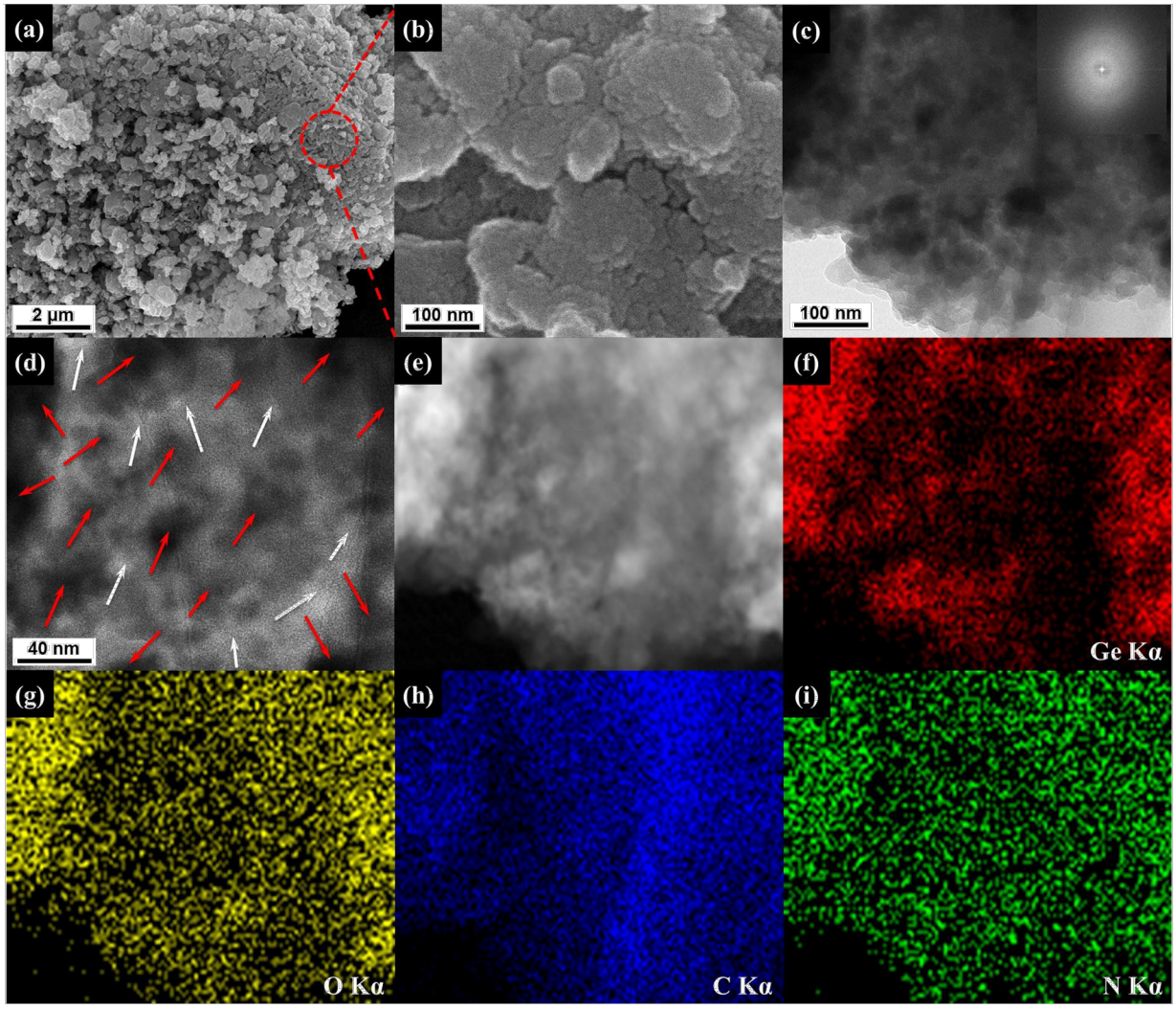

Fig. 2 Morphology of GeO_2/C: (a) Low magnification and (b) high magnification SEM images; (c,d) low magnification and high magnification TEM images, inset Fig. 2c shows the SAED pattern. The white and red arrows in Fig. 2d indicate the carbon layer and germanium nanoparticles, respectively. (e) STEM image corresponding to Fig. 2c and relevant TEM-EDS elemental mapping images of (f) Ge, (g) O, (h) C and (i) N.

measured. As shown in Fig. S3a†, the GeO_2/C had a specific area of 15.4 m^2 g^{-1}, the average pore diameter of 56 nm, and the pore volume of 0.22 cm^3 g^{-1}. For the electrode material, the pore diameter and pore volume are very important, especially in the case of materials such as Si, Ge, and Sn, which show very large volume expansion by lithiation. The large pore size enables fast Li transfer and enhances lithium diffusion inside the bulk particles. Meanwhile, pore volumes provide the housing needed for the expansion of anode material during cell operation. Hence, the anode material can operate efficiently and stably. GeO_2/C with a large pore diameter and pore volume, synthesized using the citric gel method in this study, showed satisfactory characteristics for lithium storage, as will be described in the following sections.

Fig. 2a-b displays the SEM images of the synthesized GeO_2/C. The amorphous GeO_2/C composite exhibited large

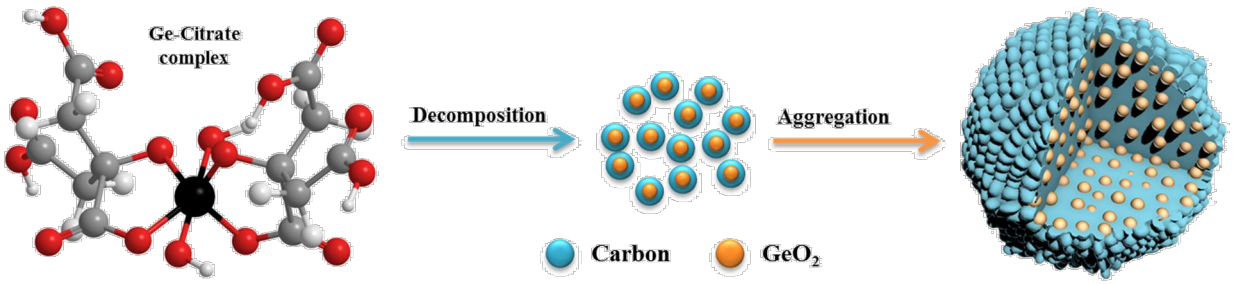

Fig. 3 Schematic for the formation of GeO_2/C from germanium citrate complex

agglomerates composed of small particles. Fig. 2c presents a low magnification TEM image of GeO_2/C. The dense, darker area indicates GeO_2 and the lighter area indicates carbon. In the TEM image, the agglomeration of GeO_2, inducing the formation of large dense particles, was also observed. The selected area electron diffraction (SAED) pattern displays diffuse scattering (inset in Fig. 2c), suggesting that the GeO_2 exist under amorphous structure, which is in good agreement with XRD pattern. Fig. 2d shows high-resolution TEM image. The amorphous GeO_2 were found to be embedded in a carbon matrix. However, the lattice spacing of GeO_2 is not observed, indicating its amorphous nature. This result is absolutely consistent with the obtained XRD results (Fig. 1a). The scanning transmission electron microscopy (STEM) image shows the homogeneous distribution of Ge in the GeO_2/C sample (Fig. 2e). Besides, from TEM- EDS elemental mapping images of GeO_2/C given in Fig. 2f-i, the presence of elements such as Ge, carbon, oxygen, and nitrogen is identified. More interestingly, all these elements are overlapped uniformly across the entire sample suggesting the uniform distribution of each element in resulted GeO_2/C.

Fig. 4 Cyclic voltammograms for (a) CB-GeO_2/C (with carbon black additive) and (b) GeO_2/C (without carbon black) electrodes at the scan rate of 0.05 mV s^{-1}.

The formation of amorphous GeO_2 embedded in the carbon buffer layer is depicted in Fig. 3. At high temperature, the side group of the complex was decomposed to release CO_2, H_2O, and the formation of GeO_2/C. The structure of GeO_2 embedded in the carbon buffer matrix has many advantages. (i) Since GeO_2 is embedded in the carbon matrix, the pulverization of GeO_2 will be avoided;[27, 28, 40, 41](ii) Although the particle size of GeO_2 is very fine, the specific area of GeO_2/C is not excessively high due to the specific area of GeO_2/C determined by the surface of carbon matrix. Thus, unique structure of GeO_2/C not only provides a shorter pathway for lithium insertion-desertion, but also decreases the irreversible capacity by preventing the direct formation of the solid electrolyte interface (SEI) layer on the surface of GeO_2;[42, 43](iii) By embedding GeO_2 in the carbon matrix, the electrical contact among the GeO_2 particles is always retained by the interconnection of the carbon matrix during cell operation, which can improve the performance of cell even at high rate of charge-discharge.[28, 44]As a result, the structure mentioned above is preferred.

Cyclic voltammetry (CV) was used to investigate the lithium insertion-desertion mechanism in the electrode. The derived cyclic voltammograms are plotted in Fig. 4. During the cathodic scan in the first cycle for the CB-GeO_2/C (with carbon black additive) electrode, a shoulder at 1.06 V was ascribed to the formation of SEI layer, and peak at 0.86 V was supposedly related to the formation of Ge and LiO_2 (Reaction 1).[26] Three overlapping reduction peaks appeared below 0.52 V in the first cathodic sweep, as shown in Fig. 4a, corresponding to formation of the Li_xGe alloy (Reaction 2).[13, 26, 35] From the second cycle, the intensity of the cathodic peaks observed around 0.86 V was significantly reduced, indicating the diminution in the rate of Reaction 1. For the GeO_2/C (without carbon black) electrode, during the cathodic scan in the first cycle, the current started to increase at around 1.02 V, as shown in Fig. 4b, which is representative of the formation of SEI layer and reduction of GeO_2 to Ge and Li_2O. The cathodic peak in the first cycle observed below 0.52 V corresponds to lithiation to form Li_xGe. The various alloys can be formed according to the reaction (Reaction 2).

$$GeO_2 + 4\,Li \rightarrow 2Li_2O + Ge \quad (1)$$

$$Ge + xLi \rightarrow (LiGe, Li_9Ge_4, Li_{16}Ge_5, Li_{15}Ge_4, Le_{17}Ge_4, Li_{22}Ge_5) \quad (2)$$

Consequently, during the anodic scan for the CB-GeO_2/C electrode, an anodic peak was observed at around 0.41 V as a result of lithium de-alloying. In addition, the peak at around 1.10 V corresponding to the reverse reaction of Reaction 1[26, 45] to form Ge-O was observed as shown in Fig. 4a. However, the peak appearing at 1.10 V for the CB-GeO_2/C electrode, corresponding to the reverse reaction of Reaction 1, was not observed for the GeO_2/C electrode without the carbon black additive (Fig. 4b). The disappearance of this peak may be attributed to the irreversibility of Reaction 1 for the GeO_2/C electrode. According to Kim et al.,[45] the presence of Cu facilitated Reaction 1 to become reversible, which improved the Coulombic efficiency in the first cycle. In the electrochemical aspect, Reaction 1 is considered to be quasi-reversible. In this study, the electrode fabricated with carbon black (CB-GeO_2/C) also showed reversibility of the Reaction 1. The carbon black appears to exhibit a similar effect to that of Cu to facilitate the re-oxidation of Ge. The role of carbon black as a catalyst was shown in the electrochemical impedance spectroscopy result in Fig. S4†. Obviously, for the CB-GeO_2/C electrode, the presence of carbon black decreased the activation energy significantly. The activation energy decreased by 0.077 eV after adding carbon black to GeO_2/C; in specifically, from 0.552 eV for the GeO_2/C electrode to 0.475 eV for the CB-GeO_2/C electrode (Table S2†). The decrease in the activation energy for the charge transfer reaction in the presence of carbon black evidently indicates the role of carbon black as a catalyst in the investigated electrodes.

Fig. 5a shows the reversible specific capacities of GeO_2/C and CB-GeO_2/C electrodes calculated based on the weight of the only active material (GeO_2) at the rate of C/2 (550 mA g^{-1}). In the first cycle, the capacity of the CB-GeO_2/C electrode reached

up to 1115 mA h g^{-1}, which was much higher than that of the GeO_2/C electrode (704 mA h g^{-1}). This can be ascribed to the promoted reversible Reaction 1 by the catalytic action of carbon black in the electrode. However, the capacity of the CB-GeO_2/C electrode decreased rapidly; after 400 cycles, the capacity decreased by about 28% compared with its initial capacity. The extremely large capacity fading of the CB-GeO_2/C electrode is attributed to the inhibition of carbon black catalysis caused by the formation of the SEI layer. The growth of the SEI layer on the surface of the carbon black appears to prevent Reaction 1 becoming reversible. Further, the contact loss between the active material and the current collector resulting from the extremely large volume change of the active material during the repeated charging/discharging is another reason for the capacity fading. Interestingly, for the GeO_2/C electrode, the specific capacity gained the highest value of 914 mA h g^{-1} after 252 cycles and the capacity decayed by only 4.7% compared with the maximum capacity, even after 400 cycles. The high specific capacity of GeO_2/C is attributed to the uniformity of the nano-size GeO_2, providing a short pathway for lithium diffusion and allowing for full lithium accessibility, resulting high practical capacity.

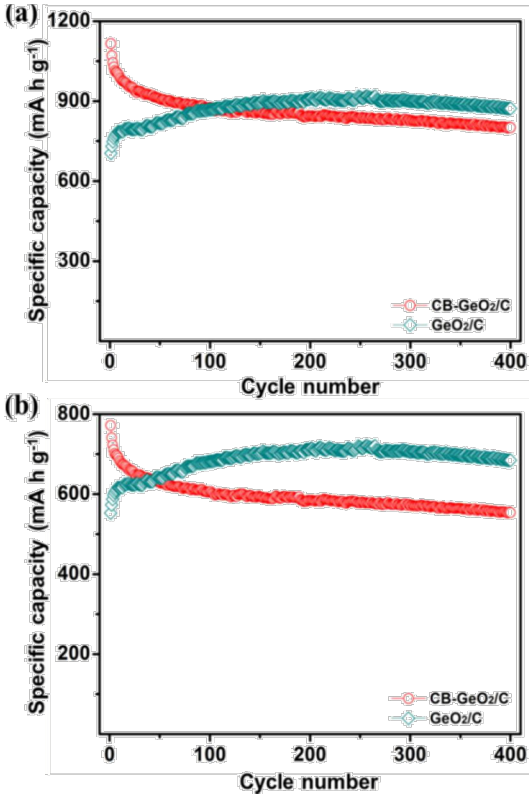

Fig. 5 Reversible specific capacities of CB-GeO_2/C and GeO_2/C electrodes calculated based on the weight of (a) only active material (GeO_2) and (b) total weight of electrode materials (GeO_2/C, carbon black and binder), respectively.

In addition, the ultra-cyclability of GeO_2/C is the result of the co-effect of the carbon matrix as well as the amorphous structure of GeO_2. The carbon matrix accommodates the expansion of GeO_2 during cycling; the structure of the GeO_2/C composite is therefore robust during cycling. Meanwhile, the amorphous GeO_2 eliminates the anisotropic expansion, that caused the structure failure.[32] Fig. 5b shows the cyclability of the CB-GeO_2/C and GeO_2/C electrodes calculated based on the total weight of electrode materials (included GeO_2/C, carbon black, and binder). As the weight content of GeO_2 in the GeO_2/C electrode is higher than that of in the CB-GeO_2 electrode, the capacity of the GeO_2/C electrode appears to be much higher than that of the CB-GeO_2/C electrode. The electrochemical performance of as-prepared GeO_2/C was also examined for comparison (Fig. S6†). The specific capacity of GeO_2/C after graphitization was remarkably larger than that of as-prepared GeO_2/C. Considering the galvanostatic cycling results, the GeO_2/C electrode without carbon black obviously predominated over the CB-GeO_2/C electrode with carbon black. To clarify the main cause of contact loss resulting in the capacity fading, the visible changes on the surface of the electrodes after 400 full charge-discharge cycles is shown in Fig. S7† and Fig. S8†. After 400 cycles, the CB-GeO_2/C electrode exhibited local exfoliation on the surface while the phenomenon hardly occurred for the GeO_2/C electrode (Fig. S7†). Originally, the SEM image of the as prepared CB-GeO_2/C electrode containing carbon black showed a smoother surface (Fig. S8a†) than that of the GeO_2/C electrode without carbon black (Fig. S8b†), since fine carbon black particles could fill the interstices in the CB-GeO_2/C electrode. It is worth noting that some cracks appeared on the surface of electrode due to the higher specific area of carbon black. The specific surface area of the CB-GeO_2/C powder, 144.6 m^2 g^{-1}, was higher than that of the GeO_2/C powder (15.4 m^2 g^{-1}, calculated from Fig. S3†); hence, a thin layer of binder was formed on the surface of the electrode active material. Therefore, the adherence among grains of CB-GeO_2/C in the electrode weakened compared to that of the sample GeO_2/C. Thus, after drying at 100 °C for 6h, the electrode material shrank and left cracks on the surface of electrode. In contrast, a thicker binder layer on the active materials of the GeO_2/C electrode enabled stronger bonding among active materials and the current collector. Accordingly, the GeO_2/C electrode could be more stable during charge-discharge cycling and exhibited the better cyclability. Moreover, due to strong bonding between binder and active material in the GeO_2/C electrode, more time was required to activation, and the highest specific capacity obtained after 252 cycles. After 400 cycles, the CB-GeO_2/C and GeO_2/C electrodes showed a slight change in the surface of the electrodes (Fig. S8c-d†). The electrode surfaces are thought to be covered with a thin SEI layer, which can render the appearance of the surface of the electrode to be smooth and compact. The formation of the SEI layer due to the decomposition of the electrolyte on the electrode surface during cycling caused an increase in the solution resistance (Fig. S9† and Table S3†).

Galvanostatic cyclic charge-discharge profiles for the CB-GeO_2/C and GeO_2/C electrodes are shown in Fig. 6. In the first discharge cycle, both the CB-GeO_2/C and GeO_2/C electrodes exhibited a high discharge capacity close to 2220 mA h g^{-1}. However, the charge capacity of CB-GeO_2/C (1115 mA h g^{-1}), was higher than that of GeO_2/C (704 mA h g^{-1}). The large irreversible capacity of the GeO_2/C and CB-GeO_2/C electrodes is attributed to the formation of Li_2O during the discharge process and formation of SEI layer, which induced a low Coulombic efficiency in the first cycle. As shown in Fig. S10†, the Coulombic efficiency of the GeO_2/C electrode in the first cycle was about 31.9%. Nevertheless, in the second cycle, the Coulombic efficiency suddenly increased to 95.4% and from the 15th cycle, the Coulombic efficiency reached approximately 100%.

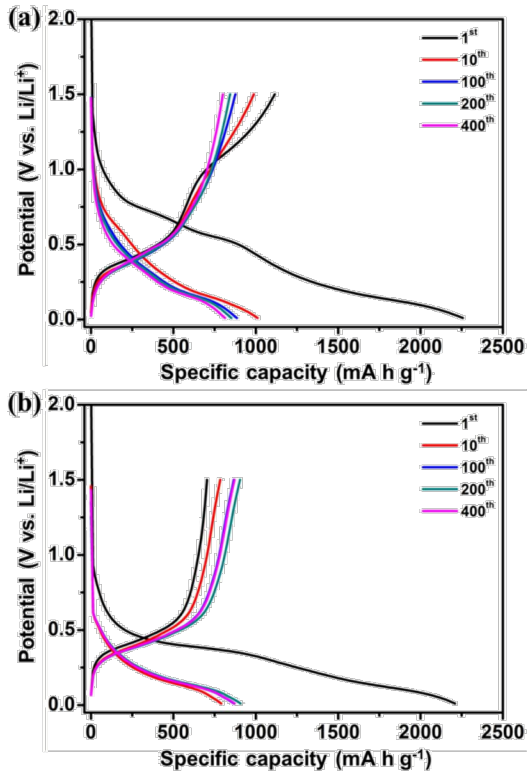

Fig. 6 Galvanostatic charge-discharge profiles for (a) CB-GeO_2/C and (b) GeO_2/C electrodes under C/2 rate in the potential rage from 0.01 to 1.5 V vs. Li/Li^+.

Although the Coulombic efficiency of the GeO_2/C electrode in the first cycles was lower than that of the CB-GeO_2/C electrode (49.4%), from the next cycles the GeO_2/C electrode predominated over the CB-GeO_2/C electrode by exhibiting a higher Coulombic efficiency. This behaviour may be explained by the smaller surface area of the GeO_2/C electrode compared to that of the CB-GeO_2/C electrode; it is known that the SEI layer is formed on the surface of the material, so increasing the specific area will increase the irreversible capacity, which is consumed for the formation of the SEI layer.[28, 46] The low Coulombic efficiency of the GeO_2/C electrode in the first cycle can be a problem for practical application. However, the Coulombic efficiency of the electrode can be improved by adding extra sacrificial lithium to the anode to improve the initial efficiency.[47, 48]

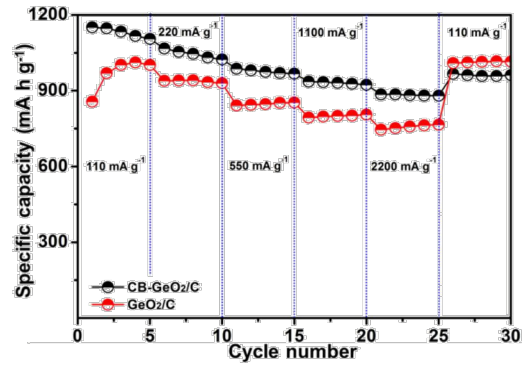

Fig. 7 Rate capability of CB-GeO_2/C and GeO_2/C electrodes under different charge-discharge rates for each 5 cycles in the potential range of 0.01 ~ 1.5 V vs. Li/Li^+, respectively.

Fig. 7 shows the rate capability of the CB-GeO_2/C and GeO_2/C electrodes for each of the 5 cycles under different charge-discharge rates. Within first 25 cycles when the charge-discharge rate was increased from 110 to 2200 mA g^{-1}, the CB-GeO_2/C exhibited higher specific capacity than that of GeO_2/C. This is attributed to the presence of carbon black as referred above. However, in comparison with CB-GeO_2/C, GeO_2/C still exhibited the slightly dominant rate capability. In particular, the capacity of the GeO_2/C electrode under the rate of 2200 mA g^{-1} was about 76.4% of the capacity measured under the rate of 110 mA g^{-1}. When the charge-discharge rate returned to the initial rate of 110 mA g^{-1}, the capacity rapidly reached 1009 mA h g^{-1}, which was even higher than that of the first 5 cycles measured under the rate of 110 mA g^{-1}. In contrast, for the CB-GeO_2/C electrode, the capacity measured under the rate of 2200 mA g^{-1} was about 76.9% of the capacity measured under the rate of 110 mA g^{-1}. When the charge-discharge rate returned to the initial value of 110 mA g^{-1}, the capacity gained only about 83.5% of the initial value. This is due to the specific capacity of CB-GeO_2/C continuously declining with the cycle number. From 26th cycle, at the low rate of 110 mA g^{-1} the specific capacity of GeO_2/C was larger than that of CB-GeO_2/C. This demonstrates that, the GeO_2/C showed the better rate capabilities even undergo the high charge-discharge rate. In summary, the formation of the carbon layer covering the GeO_2 particles during the synthesis process probably improved the conductivity of the GeO_2/C composite, resulting in enhancing the performance of the cell under the high charge-discharge rate. Accordingly, even without carbon black the GeO_2/C composite electrode showed better performance under a high charge-discharge rate.

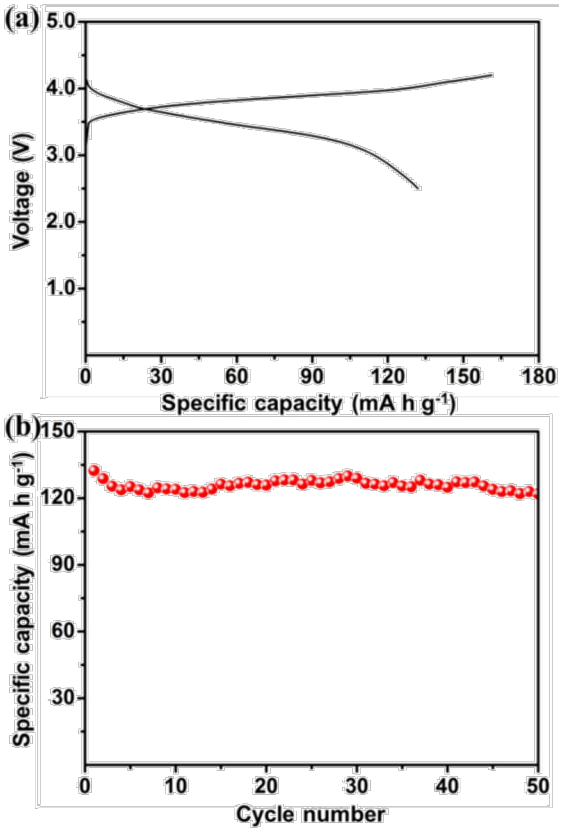

Fig. 8 (a) Charge-discharge profile at first cycle and (b) cyclability of the full cell composed of GeO_2/C anode and $LiCoO_2$ cathode, measured at the C/2 rate.

To check the practical applicability of the GeO_2/C electrode in secondary lithium ion batteries, a full cell was assembled. Specifically, the GeO_2/C anode was coupled with a commercial $LiCoO_2$ cathode. The full cell was tested in the cell potential range of 2.5 ~ 4.2 V. As shown in Fig. 8a, the full cell exhibited the discharge and charge capacity of 132 mA h g^{-1} and 161 mA h g^{-1}, respectively, and the Coulombic efficiency of 82% in the first cycle under the C/2 rate (the capacity was calculated based on the weight of the $LiCoO_2$ cathodic material). In addition, the full cell exhibited the cyclability as shown in Fig. 8b. Even after 50 cycles, the capacity of $LiCoO_2$ was reduced by only 7.6% compared with the initial capacity. Accordingly, the performance of GeO_2/C assembled in the full cell configuration demonstrated excellent reversibility and stability.

Conclusions

By using the facile sol-gel synthesis method, the amorphous GeO_2/C composite was prepared. The intrinsic structure of nano GeO_2 embedded in the carbon matrix was obtained. The carbon present in the composite of GeO_2/C as a buffer layer as well as a conductive agent not only increased the weight ratio of the GeO_2 active material in the electrode, but also improved the cyclability of the electrode employing the GeO_2/C. Even after 400 cycles, the capacity decayed by only 4.7% compared with the maximum capacity. In contrast, the addition of carbon black as a conducting additive in the electrode (CB-GeO_2/C) improved the reversibility of the formation of Li_2O by acting as a catalyst for the reversible reaction. However, the presence of carbon black decreased the weight ratio of GeO_2 in the electrode and additionally induced the capacity fading of the electrode. Due to the structure of the nano GeO_2 embedded in the carbon matrix, the conductivity of GeO_2/C composite electrode was improved and the rate capability of the GeO_2/C electrode was comparable to that of the CB-GeO_2/C electrode. The capacity of GeO_2/C and CB-GeO_2/C electrodes under the rate of 2200 mA g^{-1} was as much as about 76% of their initial capacity measured under the rate of 110 mA g^{-1}. The full cell composed of GeO_2/C anode and commercial $LiCoO_2$ cathode showed a high Coulombic efficiency of 82% in the first cycle, and superior cyclability. The capacity retention of $LiCoO_2$ was established to be 92.4%, even after 50 cycles.

Acknowledgements

This work was supported by the MOE, Korea, under the National Research Foundation of Korea (NRF) grant (No. 2012R1A2005977) and by the Ministry of Science, ICT & Future Planning (MSIP), Korea, under the Convergence Information Technology Research Center (C-ITRC) support program (NIPA-2013-H0301-13-1009) supervised by the National IT Industry Promotion Agency (NIPA).

Notes and references

Department of Materials Science and Engineering, Chonnam National University, 77, Yongbongro, Bukgu, Gwangju 500-757, South Korea
Tel: +82-62-530-1704; Fax: +82-62-530-1699
E-mail address: parkcj@jnu.ac.kr

† Electronic Supplementary Information (ESI) available: FTIR of GeO_2/C; N_2 adsorption/desorption of the GeO_2/C and the mixture GeO_2/C and carbon black; Electrochemical impedance spectroscopy (EIS); The Arrhenius plot for CB-GeO_2/C and GeO_2/C electrodes; The activation energy for CB-GeO_2/C and GeO_2/C electrodes; Raman spectroscopy and electrochemical performance of as prepared GeO_2/C; The surface morphology of samples after cycling; Coulombic efficiency; SEM image of electrodes before and after cycling.

References

1. C.-M. Park, J.-H. Kim, H. Kim and H.-J. Sohn, *Chemical Society Reviews*, 2010, **39**, 3115-3141.
2. A. S. Arico, P. Bruce, B. Scrosati, J.-M. Tarascon and W. van Schalkwijk, *Nat Mater*, 2005, **4**, 366-377.
3. J.-U. Seo and C.-M. Park, *Journal of Materials Chemistry A*, 2013, **1**, 15316-15322.
4. A. Magasinski, P. Dixon, B. Hertzberg, A. Kvit, J. Ayala and G. Yushin, *Nat Mater*, 2010, **9**, 353-358.
5. J. Shin, K. Park, W.-H. Ryu, J.-W. Jung and I.-D. Kim, *Nanoscale*, 2014.
6. X. Feng, J. Yang, Y. Bie, J. Wang, Y. Nuli and W. Lu, *Nanoscale*, 2014.
7. X. Li, J. Liang, Y. Zhu, Z. Hou, Y. Wang and Y. Qian, *Chemical Communications*, 2014.
8. C. Kim, M. Ko, S. Yoo, S. Chae, S. Choi, E.-H. Lee, S. Ko, S.-Y. Lee, J. Cho and S. Park, *Nanoscale*, 2014, **6**, 10604-10610.
9. M. W. Forney, M. J. Dzara, A. L. Doucett, M. J. Ganter, J. W. Staub, R. D. Ridgley and B. J. Landi, *Journal of Materials Chemistry A*, 2014, **2**, 14528-14535.
10. S. Wu, R. Wang, Z. Wang and Z. Lin, *Nanoscale*, 2014, **6**, 8350-8358.
11. M. Liu, X. Ma, L. Gan, Z. Xu, D. Zhu and L. Chen, *Journal of Materials Chemistry A*, 2014.
12. L. Ouyang, L. Guo, W. Cai, J. Ye, R. Hu, J. Liu, L. Yang and M. Zhu, *Journal of Materials Chemistry A*, 2014, **2**, 11280-11285.
13. Y. Xiao, M. Cao, L. Ren and C. Hu, *Nanoscale*, 2012, **4**, 7469-7474.
14. Y.-D. Ko, J.-G. Kang, G.-H. Lee, J.-G. Park, K.-S. Park, Y.-H. Jin and D.-W. Kim, *Nanoscale*, 2011, **3**, 3371-3375.
15. M. V. Reddy, G. V. Subba Rao and B. V. R. Chowdari, *Chemical Reviews*, 2013, **113**, 5364-5457.
16. P. Su, S. Liao, F. Rong, F. Wang, J. Chen, C. Li and Q. Yang, *Journal of Materials Chemistry A*, 2014.
17. J. Yue, X. Gu, L. Chen, N. Wang, X. Jiang, H. Xu, J. Yang and Y. Qian, *Journal of Materials Chemistry A*, 2014.
18. H. S. Jadhav, R. S. Kalubarme, C.-N. Park, J. Kim and C.-J. Park, *Nanoscale*, 2014, **6**, 10071-10076.
19. H. Kageyama, Y. Oaki and H. Imai, *RSC Advances*, 2014, **4**, 44124-44129.
20. F. Wu, Z. Wang, X. Li and H. Guo, *RSC Advances*, 2014, **4**, 40111-40119.
21. Y.-M. Lin, K. C. Klavetter, A. Heller and C. B. Mullins, *The Journal of Physical Chemistry Letters*, 2013, **4**, 999-1004.
22. Y. Son, M. Park, Y. Son, J.-S. Lee, J.-H. Jang, Y. Kim and J. Cho, *Nano Letters*, 2014, **14**, 1005-1010.
23. J. Graetz, C. C. Ahn, R. Yazami and B. Fultz, *Journal of The Electrochemical Society*, 2004, **151**, A698-A702.
24. A. M. Chockla, K. C. Klavetter, C. B. Mullins and B. A. Korgel, *ACS Applied Materials & Interfaces*, 2012, **4**, 4658-4664.
25. N. Nitta and G. Yushin, *Particle & Particle Systems Characterization*, 2014, **31**, 317-336.
26. J. S. Peña, I. Sandu, O. Joubert, F. S. Pascual, C. O. Areán and T. Brousse, *Electrochemical and Solid-State Letters*, 2004, **7**, A278-A281.
27. R. A. DiLeo, S. Frisco, M. J. Ganter, R. E. Rogers, R. P. Raffaelle and B. J. Landi, *The Journal of Physical Chemistry C*, 2011, **115**, 22609-22614.
28. K. H. Seng, M.-h. Park, Z. P. Guo, H. K. Liu and J. Cho, *Nano Letters*, 2013, **13**, 1230-1236.
29. L. Xiao, Y. Cao, J. Xiao, W. Wang, L. Kovarik, Z. Nie and J. Liu, *Chemical Communications*, 2012, **48**, 3321-3323.
30. L. P. Tan, Z. Lu, H. T. Tan, J. Zhu, X. Rui, Q. Yan and H. H. Hng, *Journal of Power Sources*, 2012, **206**, 253-258.
31. Y. Idota, T. Kubota, A. Matsufuji, Y. Maekawa and T. Miyasaka, *Science*, 1997, **276**, 1395-1397.

32. S. W. Lee, M. T. McDowell, J. W. Choi and Y. Cui, *Nano Letters*, 2011, **11**, 3034-3039.
33. V. Palomares, A. Goñi, I. G. d. Muro, I. de Meatza, M. Bengoechea, I. Cantero and T. Rojo, *Journal of Power Sources*, 2010, **195**, 7661-7668.
34. M. E. Spahr, D. Goers, A. Leone, S. Stallone and E. Grivei, *Journal of Power Sources*, 2011, **196**, 3404-3413.
35. W. Li, Z. Yang, J. Cheng, X. Zhong, L. Gu and Y. Yu, *Nanoscale*, 2014, **6**, 4532-4537.
36. W. Li, X. Wang, B. Liu, J. Xu, B. Liang, T. Luo, S. Luo, D. Chen and G. Shen, *Nanoscale*, 2013, **5**, 10291-10299.
37. X. Zhou, Z. Dai, S. Liu, J. Bao and Y.-G. Guo, *Advanced Materials*, 2014, **26**, 3943-3949.
38. Y. Kanno and J. Nishino, *J Mater Sci Lett*, 1993, **12**, 110-112.
39. A. C. Ferrari and J. Robertson, *Physical Review B*, 2000, **61**, 14095-14107.
40. Y. Wang and G. Wang, *Chemistry – An Asian Journal*, 2013, **8**, 3142-3146.
41. Y. Chen, C. Yan and O. G. Schmidt, *Advanced Energy Materials*, 2013, **3**, 1269-1274.
42. B. Liu, P. Soares, C. Checkles, Y. Zhao and G. Yu, *Nano Letters*, 2013, **13**, 3414-3419.
43. G. Zheng, S. W. Lee, Z. Liang, H.-W. Lee, K. Yan, H. Yao, H. Wang, W. Li, S. Chu and Y. Cui, *Nat Nano*, 2014, **9**, 618-623.
44. Y. Xu, Q. Liu, Y. Zhu, Y. Liu, A. Langrock, M. R. Zachariah and C. Wang, *Nano Letters*, 2013, **13**, 470-474.
45. C. H. Kim, Y. S. Jung, K. T. Lee, J. H. Ku and S. M. Oh, *Electrochimica Acta*, 2009, **54**, 4371-4377.
46. Y.-S. Han, J.-H. Jung and J.-Y. Leec, *Journal of The Electrochemical Society*, 2004, **151**, A291-A295.
47. J. Hassoun, S. Panero, P. Reale and B. Scrosati, *Advanced Materials*, 2009, **21**, 4807-4810.
48. C. Chae, H.-J. Noh, J. K. Lee, B. Scrosati and Y.-K. Sun, *Advanced Functional Materials*, 2014, **24**, 3036-3042.